# Visible light emissions and single-electron tunneling from silicon quantum dots embedded in Si-rich SiO$_2$ deposited in plasma phase

Keunjoo Kim

*OPTEL Semiconductor Corporation, Iksan 570-210, Korea*

Visible photoluminescence at room temperature was observed in silicon-rich oxide films deposited by an electron cyclotron resonance plasma with a mixture of silane and oxygen. The photocurrent measurement also exhibits evidence of stable luminescence at 3.0- and 2.2-eV bands from the silicon-enriched parts of oxide films. The emission energy range corresponds to a crystallite size of 10–35 Å. A model of the quantum dot is suggested from an infrared spectroscopic measurement of the chemical bond structures of oxide films. The stable light emissions from both the as-deposited and the rapid thermal annealed samples are related to the oxygen passivation of grain boundaries in the Si nanocrystallites. The current-voltage measurement for Si-rich oxides shows discontinuous currents around zero voltage at room temperature. The jump of the conductance relates to the Coulomb blockade in the array of Si quantum dots. [S0163-1829(98)04620-7]

Nanoscale crystalline structures have attracted considerable attention in the development of silicon-compatible quantum devices, but the low quantum efficiency of indirect band-gap materials such as Si and Ge has limited their use in optoelectronic devices. Recently, the discovery of strong luminescence spectra from porous silicon has created new possibilities for optoelectronic applications.[1] The quantum efficiency of photoluminescence (PL) for porous silicon depends on the passivation of grain boundaries in nanocrystallites. The stability of the PL for porous silicon can be significantly improved by the passivation of oxygen through rapid thermal processing.[2,3] Furthermore, the electrical property of the nanostructure is highlighted by the quantum transport of single-electron tunneling, which is a noble phenomenon useful for applications in single-electron transistors.

The PL from quasiisolated silicon clusters with oxidized grain surfaces embedded in an SiO$_2$ matrix has been established.[4,5] Si particles may be embedded by conventional rf-magnetron sputtering by varying the substrate temperature for various Si particle sizes. Another method has been suggested from the plasma-induced deposition of hydrogenated amorphous silicon films with a subsequent dry oxidation.[6] In this process, the crystallite size and the fraction of nanocrystalline silicon in the films are easy to control; however, in the preparation of samples, it is difficult to oxidize at temperatures of more than 1000 °C. The implantation of Si$^+$ ions into the SiO$_2$ layer also provides a visible PL band from the nanocrystalline phase of silicon with a subsequent rapid thermal annealing process.[7,8] From these findings, it is valuable to explore other experimental methods for the light emission process of silicon clusters surrounded by oxygen atoms.

In this work, we grew silicon-rich oxide layers with an electron cyclotron resonance (ECR) chemical vapor deposition and investigated the formation of quantum dots from optical and electrical properties. The optical emissions were also verified by photocurrent measurements. The size of the Si particles was analyzed by a diffractogram from x-ray diffraction (XRD) analysis. The current-voltage ($I$-$V$) measurement on Si-rich oxides displays discontinuous currents around zero voltage at room temperature.

Silicon-rich oxide films were deposited by the ECR plasma from a mixture of silane (SiH$_4$) and oxygen at a growth temperature of 200 °C. The ECR plasma was generated by a microwave power of 400 W. The pure oxygen gas (99.99%) supplied into the ECR plasma source activated the silane into the plasma phase. The sample used for the deposition was a boron-doped Si(100) with a resistivity of 6–9 $\Omega$ cm, which was pretreated with O$_2$ plasma in $9.5 \times 10^{-5}$ Torr for 10 min. The base pressure was $2 \times 10^{-6}$ Torr and the process pressure was $9 \times 10^{-5}$ Torr. The thickness of the deposited films was around 800 nm. The rapid thermal annealing (RTA) treatment was performed at a temperature of 900 °C for 4 min.

The oxide films were used in the investigation of room-temperature PL using the 325-nm (3.81 eV) excitation line of a He-Cd laser (IK 5451R-E, Kimmon Electric Co.) with a power of 50 mW. The luminescence was detected with a 500-mm grating monochrometer (Jarrel Ash, 82020) and a photomultiplier tube (RCA C3 1034). The emitted light was amplified by a lock-in amplifier (EG & G 5208) and recorded in the $X$-$Y$ plotter. The $I$-$V$ characteristics of the Si-rich oxide films were investigated by the metal-oxide-semiconductor (MOS) capacitor structure with a dimensional thickness of 800 nm and an area of 0.196 cm$^2$. The $I$-$V$ curve was obtained with a semiconductor parameter analyzer (HP4155A) with a bias loaded at an interval of 0.1 mV.

Figure 1 shows PL spectra for ECR oxide films that originate from nanostructures of isolated silicon particles during the ECR deposition of silicon-rich oxide layers. The as-deposited sample grown with the gas mixing ratio of silane to oxygen, $Q = 10/5$ (a) shows a pronounced PL peak of 405 nm (3.06 eV) with minor bands of around 510 (2.43) and 365 nm (3.4 eV). The RTA effect (b) results in an increased intensity and causes the redshift of the peak from 405 to 410 nm (3.02 eV). The PL intensity from the as-deposited sample with $Q = 10/4$ (c) shows peaks of around 398 (3.11) and 540 nm (2.29 eV). The quantum efficiency of the 540-nm band with a full width at a half-maximum (FWHM) of 0.344 eV is relatively higher than that of the 398 nm band with a FWHM of 0.516 eV. The overall quantum efficiency is enhanced using thermal annealing (d). The 408-nm (3.03 eV) band becomes acute with an enlarged FWHM of 0.668 eV. Furthermore, the RTA process exhibits a 398-nm peak with a
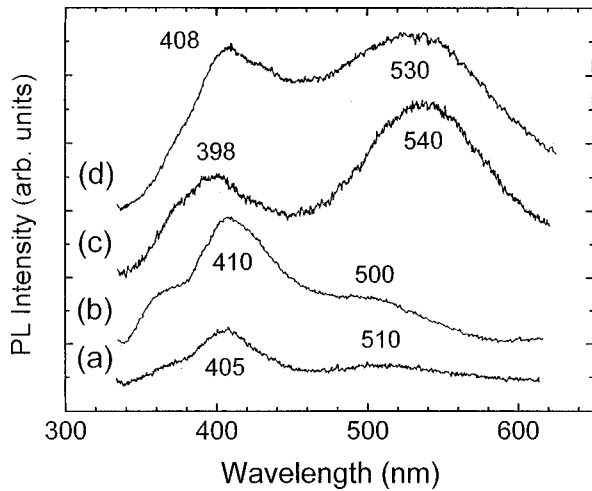
FIG. 1. PL spectra of the samples for the flow rate ratio of silane to oxygen, $Q=10/5$ (a), 10/4 (c), and the corresponding RTA treated samples (b and d). The 2.2 eV PL spectrum depends on the silicon concentration to form a large silicon cluster. A greater oxygen-deficient film exhibits a greater number of PL bands.
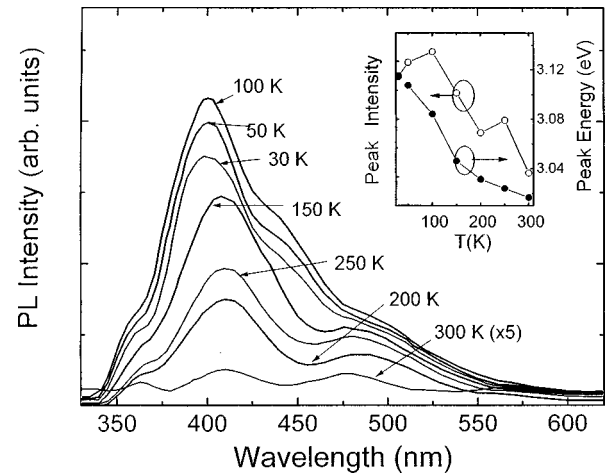


FIG. 2. The temperature dependence of PL intensity for the as-deposited sample of $Q=10/6$. Room-temperature multiple peaks merge into the envelope peaked at 402 nm, asymmetrically. In the inset, PL intensity increases with decreasing temperature similarly to the porous silicon, nonmonotonically. The main peak of the 402-nm band shows a blueshift by lowering the temperature at a coefficient of $4.2\times10^{-4}$ eV/K.

redshift of 80 meV, while the 540-nm peak exhibits a blueshift with an energy of 40 meV.

Reproducible PL spectra are highly dependent on the composition of the silane and oxygen in the chemical reaction. The $Q=10/5$ sample (a and b) shows a very low intensity at the 540-nm PL band, while the PL is obviously observed in the $Q=10/4$ sample (c and d). The $Q=10/6$ sample observed at 300 K (Fig. 2) shows four peaks at wavelengths of 363 and 402 nm (violet emissions), 475 nm (blue emission), and 557 nm (green emission). The 475-nm PL band is new and is not available for both $Q=10/4$ and 10/5 samples, which indicates that there is a certain relationship between the flow rate ratio and PL spectral bands. The resemblance of PL bands between the as-deposited and the RTA treated samples implies that their particle sizes are similar although their morphologies are changed by the RTA treatment. The core of the Si nanoparticle becomes ordered by the thermal annealing effect and enhances the quantum efficiency.

Temperature-dependent PL measurements were carried out from 30 to 300 K using He-Cd laser excitation for the $Q=10/6$ sample. The peaks show the blueshift as the temperature decreases as shown in Fig. 2. The temperature coefficient of the peaks is determined to be $4.2\times10^{-4}$ eV/K, which is close to the corresponding value of the band gap of the single crystalline Si ($4.0\times10^{-4}$ eV/K). This result suggests that violet and blue emissions arise from Si nanocrystallites but are not caused by defect levels. Zhao et al.[9] reported a similar conclusion. Their luminescence band shows separate peaks in a wavelength region from 350 to 500 nm with a temperature coefficient of $3\times10^{-4}$ eV/K. The PL intensity increases but not monotonically as the temperature is lowered. This temperature-dependent behavior of PL intensity is similar to that of porous silicon.[10] The quantum efficiency is strongly enhanced at the 402-nm band. As Kanemitsu et al. suggested,[11] the nonuniform and highly asymmetric size distribution of nanoparticles could be caused by a size step effect on a single atomic layer step,

which is used to explain multiple PL peaks in porous silicon. In addition, the intensities of peaks depend linearly on the excitation power density. These facts indicate that the observed violet and blue emissions are due to direct transitions in confined Si nanocrystallites (nc-Si).

Figure 3 shows the photocurrent (PC) injected by photon energy for the as-deposited sample of $Q=10/4$. The typical peak of the PC intensity at 1.12 eV is attributed to the silicon band gap. The cut-off PC intensity was set at $10^{-7}$ A. In general, the PC of the energy above the band gap decays exponentially in crystalline silicon. However, the ECR deposited sample with the Si-rich oxide layer shows two bands with PC intensity at 3.04 and 2.0 eV above the band gap. Since photoconductance is related to the electron density of states (DOS) on energy levels, the energy bands above the
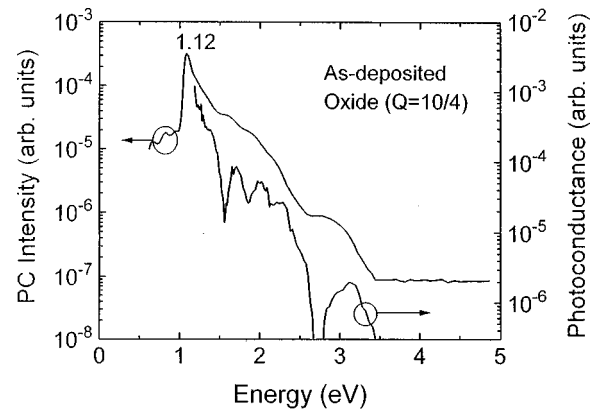


FIG. 3. The photocurrent intensity and the photoconductance of the as-deposited sample with a flow rate ratio of $Q=10/4$. The photocurrent peaked at 1.12 eV is the silicon band gap. Above the band-gap energy, the PC does not decrease exponentially, indicating the existence of quantum states. The photoconductances, corresponding to the DOS of electronic structures, peak at 3.04, 2.23, 1.98, and 1.68 eV.

silicon band gap indicate that the silicon-enriched part of the oxide layer contributes to this phenomenon and forms quantum levels. The peak of photoconductance from the 2.0 eV band is split into 1.68, 1.98, and 2.23 eV, in detail, and the 3.04 eV peak is consistent with the PL measurement.

The crystallite size was calculated by broadening in the XRD line. Since the angular range of the intensity increases as the number of planes of crystallite decreases, the width of the diffraction curve increases as the diameter of the crystallite decreases.[12] Figure 4 shows the x-ray diffractogram of the ECR deposited SiO$_2$ layer on Si(100) in terms of the double Bragg angle 2$\theta$ using the source of Mo K$_\alpha$ lines with an averaged wavelength of 0.71069 Å. The very intense peak at 30.4° is the diffraction of the (400) plane on the bare Si substrate. The intensity around 30.4° in the (400) plane of Si was broadened in the ECR oxide sample, where the profile shapes are not symmetrical at all scattering angles. This asymmetric broadening originates from the silicon-enriched part of the SiO$_2$ layer. The peak positions of XRD in ECR deposited oxide films are similar to quartz with a different tendency in intensity. It should be noted that crystalline oxides such as cristobalite and tridymite show a major peak at 17.9° in the (101) plane and quartz also shows a relatively intensive peak from the (101) plane.[13] Other SiO$_2$-related peaks are located at 26.9° (111), 31.5° (200), 37.4° (112), 55.5° (301), and 63.1° (400).

A small asymmetric broadening around the (400) plane of Si indicates that there are several peaks in the envelope of the XRD intensity. The deposited silicon-rich oxide layer is neither in the crystalline phase of the SiO$_2$ layer nor exactly in the amorphous SiO$_2$ phase. Consequently, the broadening of peaks around Si (400) implies another result like the development of the nanocrystalline Si core in the silicon-enriched parts of the oxide layer. There exists hundreds of peaks with various FWHM's near the Si(400) peak. The diameters of crystallites can be analyzed with the Scherrer
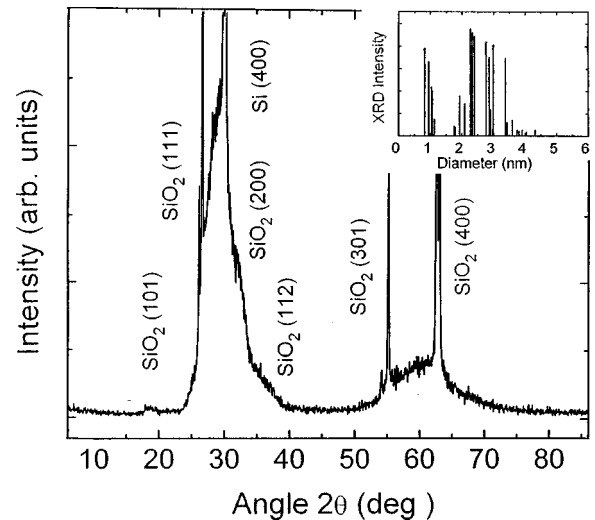


FIG. 4. The x-ray diffraction intensity for various diameters of crystallites from the ECR oxide deposited on Si(100) with a flow ratio of $Q = 10/4$. The asymmetric broadening of the XRD intensity on the bottom of the Si(400) peak produces the tiny multipeaks, which is related to the formation of Si nanoparticles during the ECR deposition of Si-rich SiO$_2$. The inset is the diameter distribution of Si particles.

formula[12,14] as shown in the inset of Fig. 4. The diameters obtained are in the range of 10–35 Å, which can be assigned to the optical energy range of 3.0–1.67 eV from the PL spectra and the PC measurement. The morphology of oxide films can be characterized using Fourier-transformation infrared (FTIR) spectroscopy.

Figure 5 shows chemical bond structures from the FTIR transmittance. The dominant absorption is due to the Si-O bonding as evidenced both in the asymmetric stretching mode at 1070 cm$^{-1}$ and in the separate lower-frequency absorption at 819 cm$^{-1}$ caused by the rocking mode in bridg-
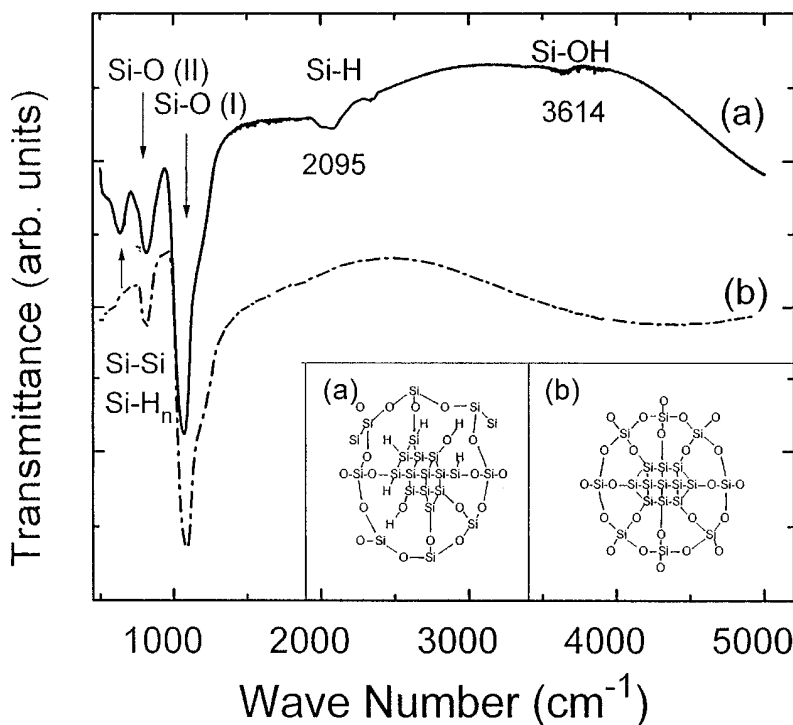


FIG. 5. The FTIR transmittance on the as-deposited Si-rich SiO$_2$ films (a) and the RTA treated film (b) for the flow rate ratio of $Q = 10/4$. The Si-O stretching mode at 1070 cm$^{-1}$ is shifted to 1074 cm$^{-1}$ by the RTA effect. The Si-H and Si-OH modes in the as-deposited sample disappear. In addition, the Si-Si wrong bond mode at 617 cm$^{-1}$ as well as the deformation mode of Si-H$_n$($n \leq 3$) at 640 cm$^{-1}$ (upward arrow) can no longer be seen in the RTA sample. The inset shows a model for quantum dot structures according to chemical bondings at the surfaces of Si dots.
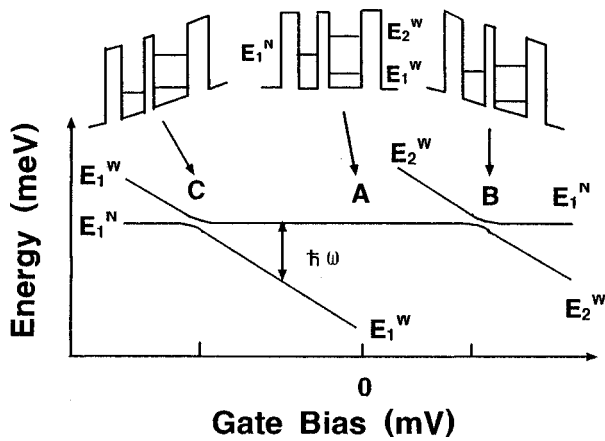
FIG. 6. Schematic of the variation of the electron-energy levels in an asymmetric double quantum dot system as a function of the applied bias. The ground states of the smaller and larger dots and the first excited state of the larger dot are denoted as $E_1^N$, $E_1^W$, and $E_2^W$, respectively. The two anticrossing resonances and the threshold for LO phonon-assisted tunneling are indicated.



FIG. 7. The $I$-$V$ curve for an Si-rich oxide in the MOS structure near zero voltage. The twofold pathways overlap between the classical Ohmic behavior and the single-electron tunneling associated with capacitive charging energy. In the inset, the corresponding derivative conductance shows the readily apparent spikes of DOS.

ing Si-O-Si bonds of the ECR deposited oxides. The FWHM of 125 $cm^{-1}$ in the Si-O stretching is larger than the stoichiometric thermal oxide case. A typical thermal oxide has a peak in the stretching mode of 1075 $cm^{-1}$ with an FWHM of 108 $cm^{-1}$. The morphology of the ECR deposited oxides is in the oxygen deficient phase. The clear resonance in the as-deposited sample (upward arrow) is shown from the deformation modes of the Si-$H_n$ ($n \leqslant 3$) at 640 $cm^{-1}$ and the Si-Si wrong bonding modes at 617 $cm^{-1}$.[15,16] Furthermore, the as-deposited sample also shows weak signals from Si-H and Si-OH bonds with three bridging oxygen atoms backbonded to the Si atom ($O_3Si$-H and $O_3Si$-OH), which occur at 2095 and 3614 $cm^{-1}$, respectively. However, the annealed sample at 900 °C shows Si-O bonds without the Si-Si wrong bond or the oxygen vacancy, Si-H, and Si-OH bonds.

Based on these chemical bondings, it is possible to speculate as to a plausible model of a quantum dot surrounded by oxygen as shown in the inset of Fig. 5. The oxygen deficiency during the ECR deposition process causes the aggregation of silicon-enriched parts in the oxide film. Hydrogen atoms are easily accumulated on the nc-Si surface as well as at the oxide/Si interface.[17] Oxygen atoms can backbond to Si atoms on the nc-Si surface because the binding energy of Si-H (3.5 eV) is much stronger than that of Si-Si (1.86 eV). The Si-H binding energy is enhanced to 4.11 eV because of the backbonded oxygen atoms.[18] The hydrogen atoms in Si-H bonds are transferred to the oxygen site in order to form a stronger bond of O-H (5.65 eV) by the plasma activation energy, which is sufficient to overcome the energy barrier.

The nc-Si surface in the as-deposited sample is passivated by the $SiO_4$ network—which includes the Si-Si wrong bond—and partially by the Si-H and Si-OH bonds. In the RTA process, the surface passivation is rearranged with the well-organized $SiO_4$ network. Similar to the PL efficiency in porous silicon,[2,3] the overall quantum efficiency increases in the RTA process because of the oxygen passivation. This may reflect an increased DOS on the nc-Si surface by the oxygen passivation rather than by the hydrogen termination. The flow rate ratio strongly correlates with PL bands. The
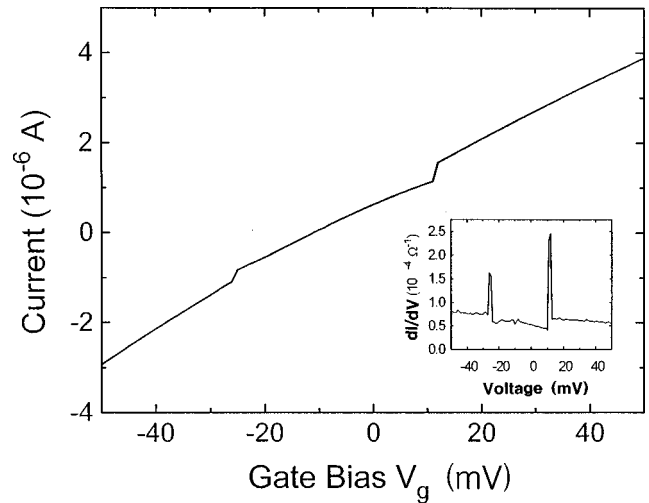
number of split bands is increased by increasing the oxygen rate, such as 398 and 540 nm for $Q = 10/4$; 365, 405, and 510 nm for $Q = 10/5$; and 363, 402, 475, and 557 nm for $Q = 10/6$. The higher flow rate of oxygen is responsible for the formation of Si quantum dots of various sizes. This indicates that the quantum size effect in the PL spectra is influenced by the flow rate ratio, which is one of the main growth factors for Si-rich $SiO_2$ films.

The Si quantum dots show an optical energy gap in the 2.2–3.0-eV range with corresponding potential barriers of 3.0–3.4 eV from a band-gap energy of 8.9 eV of $SiO_2$.[19] According to the quantum size effect of Si quantum dots embedded in the oxide layer, it is plausible to speculate the resonant tunneling mechanism of single-electron transport in a quantum dot array with various dot sizes. When the electronic states in the neighboring two dots at the same wave vector are in resonance, tunneling interaction between them leads to a splitting of these levels.[20] Figure 6 illustrates the resonant tunneling by applying appropriate positive or negative biases. For the forward bias at point $B$, the lowest electron state of the smaller dot and the first excited electron state of the relatively larger dot show a certain resonant condition for specific sizes and barrier heights of dots. For the backward bias at point $C$, the lowest electron state of both dots meets the resonant condition, which requires a very small longitudinal-optical (LO) phonon energy $\hbar\omega$.

In Fig. 7, the $I$-$V$ curve and the derivative conductance are shown in the MOS structure. The discontinuous current jumps were measured at room temperature and exhibited a phenomenon different from the conventional MOS structure. The conventional $I$-$V$ curve in an MOS structure is usually continuous, exhibiting only a very small leakage current in the dielectric oxide film which is applicable to the metal-oxide-semiconductor field-effect transistor. However, the Si-rich oxide film may have two pathways onto the electron transport: the Fowler-Nordheim tunneling mechanism, which gives the usual continuous path to the current leaking through the pure oxide layer, or the single electron tunneling
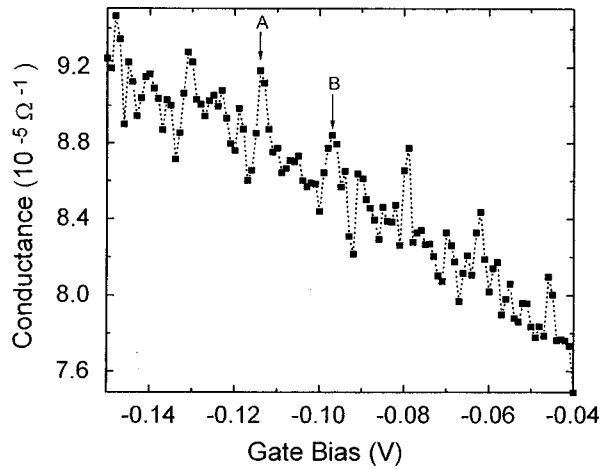
FIG. 8. The Coulomb staircase of electron conductance as a function of gate voltage of the Si quantum dots of 10–35 Å. The voltage interval is 16.65 mV corresponding to the capacitance of $C=4.8$ aF.

mechanism from the resonance phenomenon through the Si quantum dot array. At the discontinuous positions of bias voltages, the sharp increase of the conductance indicates the existence of resonant tunneling corresponding to the DOS of the energy levels in quantum dots.

For a quantum dot surrounded by an insulating oxide, an electron can be confined by the surrounding barrier of the oxide. By increasing the gate bias voltage ($V_g$), no current can flow until single-electron tunneling has occurred. The confined electron will gain the electrostatic potential energy of $e^2/2C$ corresponding to the applied energy ($eV_g$). This energy interval produces the Coulomb staircase, which is clearly shown in Fig. 8. The voltage of 16.65 mV is the

interval of points $A$ and $B$. The tunneling barrier of electrons around zero voltage is pronounced and shows the Coulomb blockade phenomenon above the Fermi contact level. For a hole to tunnel, its energy must be below the Fermi energy level.[21] Consequently, the energy gap has the width of $e^2/C$. The voltage width of 33.3 meV corresponds to the capacitance of $C=4.8$ aF (aF$=10^{-18}$ F).

However, thermal energy at room temperature requires a Coulomb blockade condition with a capacitance smaller than 3.2 aF for a single quantum dot. Of course, the value of 4.8 aF is the effective capacitance from the capacitor junctions of the array of Si quantum dots. This electron tunneling is the quantum transport with an anomalous effective number of electrons, $N_e=0.82$. This indicates that the coherent resonance tunneling in the Si dot array may overcome the thermal disturbance in spite of its slightly larger value of capacitance than the thermal limit of a single dot. The anomalous Coulomb blockade correlates with the many-body effect[22] of dot array because the exchange and correlation effect of electrons within a dot perturbs the nonlinear coherent transport through the many-body eigenstates at a temperature larger than the level broadening.

In summary, we measured the efficient visible photoluminescence spectra and the photocurrent of crystallites embedded in the Si-rich ECR oxide. The optical band gaps were measured at values of 3.0 and 2.3 eV from PL results and at values of 3.0, 2.23, 1.98, and 1.67 eV from PC results. The size of nanocrystallites was analyzed by broadening the x-ray diffraction intensity. The crystallite sizes were estimated at a range of diameters 10–35 Å. The stable and reproducible blue range of light emission from the silicon-rich oxide is related to the quantum size effect from the silicon nanoparticles surrounded by the oxide network. The anomalous Coulomb blockade around zero voltage correlates with the array of Si quantum dots with various diameters.

[1] L. T. Canham, Appl. Phys. Lett. **57**, 1046 (1990).

[2] V. Petrova-Koch, T. Muschik, A. Kux, B. K. Meyer, and F. Koch, Appl. Phys. Lett. **61**, 943 (1992).

[3] Y. Xiao, M. J. Heben, J. M. McCullough, Y. S. Tsuo, J. I. Pankove, and S. K. Deb, Appl. Phys. Lett. **62**, 1152 (1993).

[4] H. Takagi, H. Ogawa, Y. Yamazaki, A. Ishizaki, and T. Nakagiri, Appl. Phys. Lett. **56**, 2379 (1990).

[5] Y. Osaka, K. Tsunetomo, F. Toyomura, H. Myoren, and K. Kohno, Jpn. J. Appl. Phys., Part 1 **31**, L365 (1992).

[6] M. Rückschloss, B. Landkammer, and S. Veprek, Appl. Phys. Lett. **63**, 1474 (1993).

[7] T. Shimizu-Iwayama, M. Ohshima, T. Niimi, S. Nakao, K. Saitoh, T. Fujita, and N. Itoh, J. Phys.: Condens. Matter **5**, L375 (1993).

[8] P. Mutti, G. Ghislotti, S. Bertoni, L. Bonoldi, G. F. Cerofolini, L. Meda, E. Grilli, and M. Guzzi, Appl. Phys. Lett. **66**, 851 (1995).

[9] X. Zhao, O. Schoenfeld, S. Komuro, Y. Aoyagi, and T. Sugano, Phys. Rev. B **50**, 18 654 (1994).

[10] X. L. Zheng, W. Wang, and H. C. Chen, Appl. Phys. Lett. **60**, 986 (1992).

[11] Y. Kanemitsu, H. Uto, Y. Masumoto, and Y. Maeda, Appl. Phys. Lett. **61**, 2187 (1992).

[12] B. D. Cullity, *Elements of X-Ray Diffraction*, 2nd. ed. (Addison-Wesley, Reading, MA, 1978), p. 101.

[13] M. Jeyaratnam and N. G. West, in *Advances in X-Ray Analysis*, edited by C. S. Barrett, J. V. Gilfrich, R. Jenkins, T. C. Huang, and P. K. Predecki (Plenum, New York, 1989), Vol. 32, p. 585.

[14] S. Furukawa and T. Miyasato, Phys. Rev. B **38**, 5726 (1988).

[15] M. A. Tischler, K. T. Collins, J. H. Stathis, and J. C. Tsang, Appl. Phys. Lett. **60**, 639 (1992).

[16] M. H. Brodsky, M. Cardona, and J. J. Cuomo, Phys. Rev. B **16**, 3356 (1977).

[17] Z. Jing, G. Lucovsky, and J. L. Whitten, J. Vac. Sci. Technol. B **13**, 1613 (1995).

[18] Z. Jing, J. L. Whitten, and G. Lucovsky, Phys. Rev. B **45**, 13 978 (1992).

[19] D. J. DiMaria, D. W. Dong, C. Falcony, T. N. Theis, J. R. Kirtley, J. C. Tsang, D. R. Young, F. L. Pesavento, and S. D. Brorson, J. Appl. Phys. **54**, 5801 (1983).

[20] J. Shah, *Ultrafast Spectroscopy of Semiconductors and Semiconductor Nanostructures* (Springer-Verlag, Berlin, 1996), p. 272.

[21] M. A. Kastner, Rev. Mod. Phys. **64**, 849 (1992).

[22] Y. Tanaka and H. Akera, Phys. Rev. B **53**, 3901 (1996).